INORGANIC CHEMISTRY FRONTIERS

RESEARCH ARTICLE

View Article Online
View Journal | View Issue

Cite this: *Inorg. Chem. Front.*, 2021, **8**, 2542

Boosting CO_2 electroreduction to CO with abundant nickel single atom active sites†

Wei-juan Wang,[a] Changsheng Cao,[b] Kaiwen Wang *[c] and Tianhua Zhou[b]

The conversion of CO_2 into value-added chemicals through the electrocatalytic CO_2 reduction reaction (CO_2RR) is considered as an up-and-coming way to facilitate the renewable closed carbon cycle and energy storage. Therefore, the development of robust and low-cost CO_2RR electrocatalysts is essential but challenging. Herein, a Ni single-atom catalyst (Ni–SAs–NC) was successfully prepared *via* a precursor assembly strategy and a subsequent one-step pyrolysis process. Characterization studies demonstrate that abundant Ni single-atom active sites with the coordination structure of Ni–N_4 are uniformly dispersed in Ni–SAs–NC, which consequently endow it with outstanding electrocatalytic CO_2RR performance. Strikingly, the as-prepared Ni–SAs–NC can selectively convert CO_2 into CO with a high faradaic efficiency of up to 98%, and can maintain the high values exceeding 90% in a wide potential range from −0.6 to −1.0 V. This work provides a new protocol to prepare high-efficiency but low-cost single-atom electrocatalysts toward the CO_2RR and other electrochemical reactions.

Received 29th January 2021,
Accepted 19th March 2021

DOI: 10.1039/d1qi00126d

rsc.li/frontiers-inorganic

1. Introduction

The rapid increase of the concentration of CO_2 in the atmosphere caused by the excessive emission of CO_2 makes the greenhouse effect a more serious concern.[1] Recently, electrochemical reduction of CO_2 into value-added chemicals and fuels using clean and renewable electricity has represented a feasible and promising method to achieve closing of the anthropogenic carbon cycle and energy storage simultaneously.[2] However, multiple proton–electron transfer processes, as well as the concomitant competitive hydrogen evolution reaction, always occur during the electrochemical CO_2 reduction reaction (CO_2RR).[3–6] Therefore, it is essential to develop highly efficient CO_2RR electrocatalysts to achieve the exclusive production of the desired products with low energy inputs. Among various reduction products, CO is suggested as one of the most economically profitable products.[7,8] Ag and Au based electrocatalysts can achieve the conversion of CO_2 into CO with high faradaic efficiency (FE) at a low overpotential.[9–11] However, the high cost and low stability severely hinder their wide applications.[12–14]

Very recently, due to the ~100% atomic availability and extraordinary physical and catalytic properties in comparison with those of their bulk counterparts, single-atom catalysts (SACs) have quickly sparked interest in electrocatalytic fields.[15–17] Numerous efforts have been devoted to explore the preparation of SACs. Remarkably, anchoring metal single atoms on nitrogen-doped carbon substrates to form the porphyrin-like (M–N_4) coordination structure is one of the most efficacious strategies to prepare high-efficiency SACs, especially the non-noble transition metal-based SACs, with satisfactory CO_2RR performance for CO production.[18–21] Jiang *et al.* demonstrated that Ni single atoms dispersed into graphene nanosheets could present a high FE of 95% for CO generation in water.[22] Daasbjerg *et al.* developed a general method to synthesize transition metal-based SACs from cheap carbon precursors. Meanwhile, they also found that the kind of metal could significantly affect the selectivity for the conversion of CO_2 to CO.[23] Moreover, due to their well-defined chemical structures, uniform heteroatom doping, and tunable morphologies, Metal-Organic Frameworks (MOFs) are usually employed as precursors or templates to synthesize SACs for the CO_2RR.[24–26] Zhang *et al.* facilely synthesized a bismuth single-atom catalyst by thermal decomposition of a Bi–MOF with dicyandiamide, which can exclusively convert CO_2 into CO with a high FE of up to 97%.[27] Although intensive efforts have been devoted to the preparation of SACs toward the CO_2RR, complicated processes and posttreatments such as acid washing are still needed. Meanwhile, it is still challenging to synthesize transition metal based SACs that can simultaneously achieve high activity and selectivity in a wide potential window for CO generation.

[a]*College of Chemistry, Fuzhou University, Fuzhou, Fujian 350108, P. R. China*
[b]*State Key Laboratory of Structural Chemistry, Fujian Institute of Research on the Structure of Matter, Chinese Academy of Sciences (CAS), Fuzhou 350002, China*
[c]*Beijing Key Lab of Microstructure and Properties of Advanced Materials, Beijing University of Technology, Beijing 100124, P. R. China.*
E-mail: 56wkw@emails.bjut.edu.cn

†Electronic supplementary information (ESI) available. See DOI: 10.1039/d1qi00126d

Herein, we successfully fabricated a single-atom Ni catalyst (Ni–SAs–NC) by a simple precursor assembly strategy and a subsequent one-step pyrolysis process. Aberration-corrected high-angle annular dark-field scanning transmission electron microscopy (HAADF-STEM) and the Fourier transformed extended X-ray absorption fine structure (FT-EXAFS) spectrum revealed that highly dense Ni active sites with the coordination structure of $Ni–N_4$ were atomically dispersed in Ni–SAs–NC. Inductively coupled plasma atomic emission spectroscopy (ICP-AES) indicated that high Ni loadings up to 2.0 wt% could be achieved. Consequently, the as-prepared Ni–SAs–NC showed excellent electrochemical performance toward the conversion of CO_2 to CO during the CO_2RR process. Specifically, the FE for CO generation can be up to 98% without any degradation in 30 h long-term electrocatalysis at −0.65 V. Moreover, the FEs for Ni–SAs–NC could be maintained exceeding 90% in a wide potential range from −0.6 to −1.0 V.

2. Experimental

2.1. Synthesis of the Ni-based polymer precursor

The Ni-based polymer precursor was prepared based on the coordination of Ni^{2+} and an organic ligand TIPA ({tris(4-(1*H*-imidazol-1-yl)phenyl)amine}), in which TIPA was synthesized according to a previous work.[28]

2.2. Synthesis of Ni–SAs–NC

A mixture of Ni–TIPA (0.20 g), TIPA (0.50 g) and commercial carbon black (CB, 0.50 g) was dispersed in 20.0 mL ethanol with stirring for 2 h. Then, the solvent was removed through rotary evaporation. Afterward, the mixture was put in a tube furnace and subjected to pyrolysis at 400 and 800 °C for 2 h in a sequential process under N_2 flow. After cooling to ambient temperature, a black powder named Ni–SAs–NC was obtained without any post-treatments.

2.3. Synthesis of NC and Ni–NPs–NC

NC was prepared similar to Ni–SAs–NC, except that Ni–TIPA was not added in the precursor. TIPA (0.50 g) and commercial carbon black (CB, 0.50 g) were dispersed in 20.0 mL ethanol with stirring for 2 h. Then, the black powder was calcined in the same way as Ni–SAs–NC. Ni–NPs–NC was prepared similar to Ni–SAs–NC, except that the precursor was prepared *via* the dispersion of $NiSO_4{\cdot}6H_2O$ (0.16 g), imidazole (0.54 g), tris(4-bromophenyl)amine (TBA, 0.96 g) and commercial carbon black (0.50 g) in 20.0 mL ethanol.

2.4. Physical characterization

Powder X-ray diffraction (PXRD) patterns were recorded on a Rigaku Dmax2500 diffractometer with Cu Kα radiation (λ = 1.54056 Å). X-ray photoelectron spectra (XPS) were obtained using an ESCALAB 250Xi X-ray photoelectron spectrometer (Thermo Fisher, ESCALAB 250Xi, Al Kα source (15 kV, 10 mA)). Ni K-edge X-ray absorption near-edge structure (XANES) and extended X-ray absorption fine structure (EXAFS) spectra were collected on the beamline 1W1B of the Beijing Synchrotron Radiation Facility (BSRF). CO_2 adsorption analysis was carried out using a Micromeritics ASAP 2020 instrument at 298 K. The content of Ni was measured by inductively coupled plasma atomic emission spectroscopy (ICP-AES, Agilent 7700s). Scanning electron microscopy (SEM) images were obtained using a field emission scanning electron microscope (JSM6700-F). Transmission electron microscopy (TEM), including high-angle annular dark field-scanning transmission electron microscopy (HAADF-STEM), images and elemental mapping images of the samples were obtained on a FEI Titan Themis spherical aberration corrected transmission electron microscope at 300 kV.

2.5. Electrochemical characterization

All electrochemical measurements were carried out in a proton membrane (Nafion 117) separated gas-tight H-type electrochemical cell, which was connected to an electrochemical workstation (CHI760E). A catalyst coated rotating disc electrode (RDE, 0.196 cm^2) or a glassy carbon electrode (GCE, 1.0 cm^2) was used as the working electrode, while a platinum net (1.0 × 1.0 cm^2) and Ag/AgCl (3 M KCl) were employed as the counter and reference electrodes, respectively. To prepare the working electrode, the catalyst ink was obtained by dispersing 5.0 mg catalyst into a solution containing 360 μL of isopropanol, 120 μL of water and 20 μL of 5 wt% Nafion solution with sonication. Then, the ink was dropped onto the surface of the RDE or GCE, and dried at ambient temperature, leading to a catalyst loading of 0.25 mg cm^{-2}. CO_2-saturated 0.5 M $KHCO_3$ (pH ≈ 7.4) was used as the electrolyte. CO_2 with a flow rate of 10.0 sccm (standard cubic centimeter per minute) was continuously fed into the electrolyte during the CO_2RR process. All measured potentials in this work were calibrated to the reversible hydrogen electrode (RHE) scale through the following formula: $E_{RHE} = E_{Ag/AgCl} + 0.197 + 0.059 \times pH$ (V). All electrochemical data in this work are based on the electrode geometric area.

2.6. Faradaic efficiency calculation

The gaseous (CO and H_2) and liquid products during the CO_2RR process were quantitatively analyzed by gas chromatography (GC-2014C, Shimadzu) and ion chromatography (CIC-D100, SHINE), respectively. The faradaic efficiency (FE) of each product was calculated as follows:[29]

$$FE_i = \frac{V_i \times N \times F}{j_{total}}$$

where V_i represents the production rate of i; N represents the number of electrons transferred for product formation (N = 2 for CO and H_2); F represents the faradaic constant (96 485 C mol^{-1}); j_{total} represents the total current density; and i represents CO or H_2.

3. Results and discussion

Fig. 1a schematically shows the synthesis procedure of Ni–SAs–NC. Initially, the Ni-based polymer precursor, named Ni–TIPA,

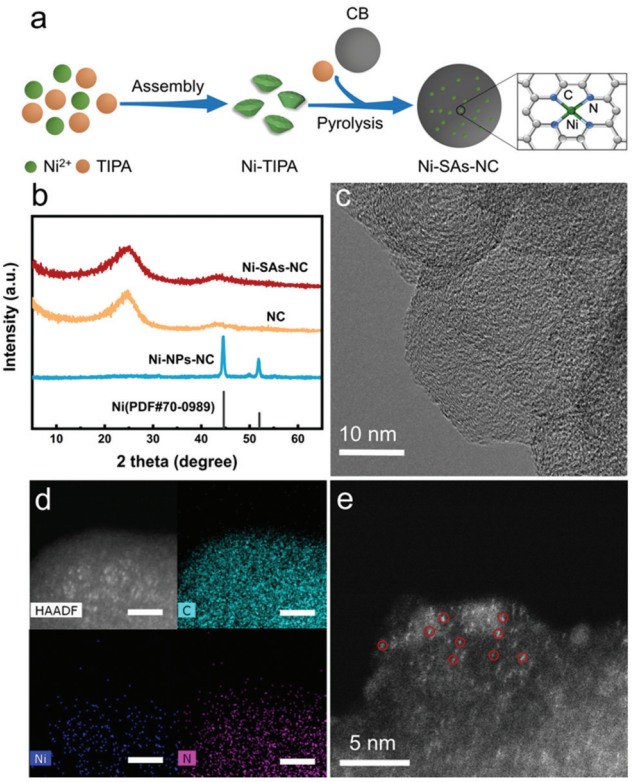

Fig. 1 (a) The schematic illustration of the preparation of Ni–SAs–NC. (b) PXRD patterns of Ni–SAs–NC, Ni–NPs–NC and NC. (c) TEM and (d) EDX elemental mapping images of Ni, C and N elements of Ni–SAs–NC (scale bar = 5 nm). (e) HAADF-STEM image of Ni–SAs–NC.

was prepared *via* the assembly of Ni^{2+} and the N-containing ligand (TIPA).[28] As shown in Fig. S1,† the prepared Ni–TIPA features a cauliflower-like morphology. Then, the mixture of Ni–TIPA, TIPA and commercial carbon black underwent one-step high-temperature pyrolysis. Finally, a black powder was obtained without any post-treatments and named Ni–SAs–NC. For comparison, the non-assembled sample Ni–NPs–NC and non-metal catalyst NC were synthesized in the same way as Ni–SAs–NC.

The powder X-ray diffraction (PXRD) pattern of Ni–SAs–NC only displays two broad diffraction peaks in ranges of 20–30° and 40–47.5° (Fig. 1b), corresponding to the C (002) and (101) planes, respectively, indicating that metallic Ni or Ni-based compounds were not generated in the as-prepared Ni–SAs–NC. In contrast, two sharp diffraction peaks at 41.6° and 52.0° were observed in Ni–NPs–NC, which are indexed well with metallic Ni (PDF#70-0989), indicating the vital role of Ni–TIPA to achieve the atomic dispersion of Ni atoms. Moreover, transmission electron microscopy (TEM) and high-resolution TEM (HRTEM) images (Fig. 1c and S2a†) confirm that no Ni clusters or nanoparticles were present in Ni–SAs–NC, which is in agreement with the PXRD pattern result. However, energy dispersive X-ray spectroscopy (EDX) elemental mapping images (Fig. 1d) illustrate that the signal of the Ni element was distributed uniformly in Ni–SAs–NC, implying that Ni might exist in Ni–SAs–NC in an atomically dispersed state. High-angle annular dark field-scanning transmission electron microscopy (HAADF-STEM) was performed to further identify the dispersion of Ni atoms in Ni–SAs–NC. As shown in Fig. 1e and S2b, c,† high-density bright dots were observed, disclosing that the single Ni atoms were dispersed on the carbon matrix uniformly. Inductively coupled plasma atomic emission spectroscopy (ICP-AES) indicates that a Ni loading of 2.0 wt% can be obtained in Ni–SAs–NC. Ni–Nps and NC substrates as its counterparts show a similar morphology (Fig. S3†). Raman spectra show two characteristic peaks located at 1344 and 1582 cm^{-1} (Fig. S4†), which correspond to the D-band and G-band of the carbon materials, respectively. However, the relative intensity ratios of the D-band and G-band (I_D/I_G) for Ni–SAs–NC, Ni–NPs–NC and NC are about 1.0, implying that the samples possess similar degrees of graphitization and disorder. Fig. S5a† shows the nitrogen adsorption–desorption isotherms of NC, Ni–SAs–NC and Ni–NPs–NC. The calculated Brunauer–Emmett–Teller (BET) surface area of Ni–SAs–NC is 210 $m^2\ g^{-1}$, which is similar to that of NC (204 $m^2\ g^{-1}$) and higher than that of Ni–NPs–NC (156.6 $m^2\ g^{-1}$), demonstrating that Ni–SAs–NC may expose more active sites. Furthermore, Ni–SAs–NC presents much higher CO_2 adsorption ability than Ni–NPs–NC (Fig. S5b†), which is beneficial for improving its CO_2RR performance.[30]

Furthermore, the surface electronic states of the samples were studied by X-ray photoelectron spectroscopy (XPS). The XPS survey spectra of Ni–SAs–NC and Ni–NPs–NC reveal the presence of Ni and N (Fig. S6a†). The detected Ni content in Ni–SAs–NC is about 2.4 wt%, which is consistent with the ICP-AES result. Then, the high-resolution XPS N 1s spectra of Ni–SAs–NC and Ni–NPs–NC were further analyzed. It can be clearly observed in Fig. S6b† that both of them can be deconvoluted into five individual peaks, corresponding to pyridinic-type N, Ni–N_x, pyrrolic-type N, graphitic-type N and oxidized-type N.[31] Table S1† shows the contents of different types of N species in Ni–SAs–NC and Ni–NPs–NC. Compared with Ni–NPs–NC, Ni–SAs–NC has a higher content of graphitic-type N species, which is beneficial for improving its CO_2RR performance.[32,33] Meanwhile, we found that the content of the Ni–N_x species in Ni–SAs–NC is much higher than that in Ni–NPs–NC, demonstrating that Ni–SAs–NC may possess more active sites for the CO_2RR. The high-resolution Ni 2p XPS spectrum of Ni–SAs–NC is shown in Fig. 2a. The peaks at around 855 and 873 eV can be attributed to the Ni $2p_{3/2}$ and Ni $2p_{1/2}$ peaks of Ni^{2+}, respectively.[34] However, the binding energies of these two peaks are slightly lower than that of Ni^{2+} in nickel phthalocyanine (NiPc), indicating that the valence state of Ni in Ni–SAs–NC is higher than 0 but lower than 2. Moreover, the X-ray absorption near-edge structure (XANES) spectrum was further applied to explore the valence state of Ni atoms in Ni–SAs–NC. As shown in Fig. 2b, the absorption edge of Ni–SAs–NC locates between Ni foil (Ni^0) and NiPc (Ni^{2+}), indicating that the valence state of Ni in Ni–SAs–NC is between 0 and 2+, which is well consistent with the XPS result.[29] In the Fourier transformed extended X-ray absorption fine structure

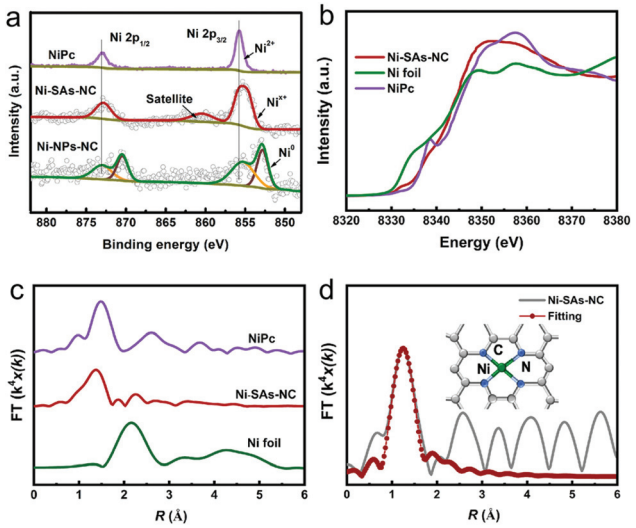

Fig. 2 (a) Ni 2p XPS spectra of NiPc, Ni–SAs–NC and Ni–NPs–NC. (b) Ni K-edge XANES spectra of Ni–SAs–NC, NiPc and Ni foil. (c) Fourier-transformed EXAFS spectra of Ni–SAs–NC, NiPc, and Ni foil. (d) Fourier-transformed EXAFS fitting results of Ni–SAs–NC (inset shows the proposed structural model of Ni–SAs–NC).

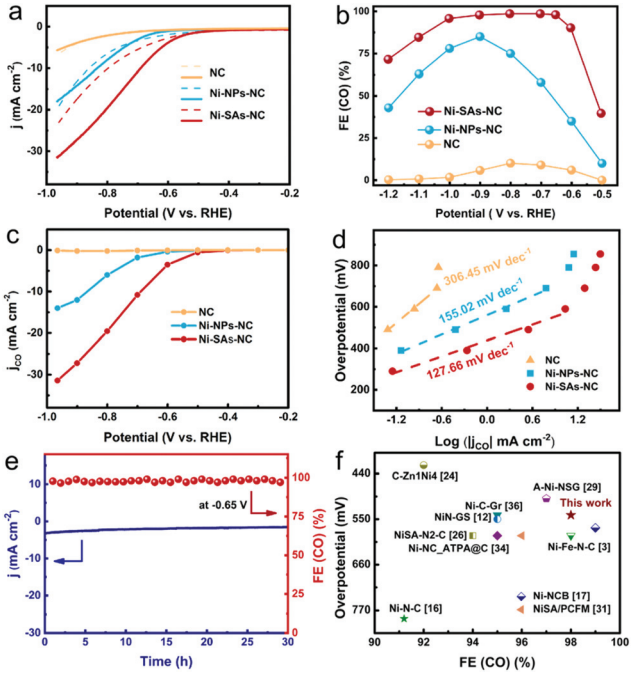

Fig. 3 (a) LSV curves of Ni–SAs–NC, Ni–NPs–NC and NC obtained on a rotating disc electrode at a rotation speed of 1600 r.m.p. and a scan rate of 5 mV s^{-1} under a CO_2 (solid lines) or N_2 (dashed lines) atmosphere. (b) Potential-dependent FEs of CO for Ni–SAs–NC, Ni–NPs–NC and NC. (c) Partial current density of CO and (d) the corresponding Tafel plots for Ni–SAs–NC, Ni–NPs–NC and NC. (e) Long-term stability test of Ni–SAs–NC at −0.65 V for 30 h. (f) Comparison of the CO_2RR performance of Ni–SAs–NC and some state-of-the-art Ni single atom catalysts.

(FT-EXAFS) spectrum (Fig. 2c), only one prominent peak at 2.16 Å representing the Ni–Ni bond is observed in Ni foil. In contrast, Ni–SAs–NC only displays the main peak at 1.40 Å, corresponding to the interaction of Ni–N, which is similar to that of NiPc,[31] revealing that the coordination environment of Ni in Ni–SAs–NC is similar to that of Ni in NiPc. The Ni EXAFS fitting curves shown in Fig. 2d and Table S2† confirm that the Ni atom in Ni–SAs–NC is coordinated by four N atoms to generate the possible Ni–N_4 structure, which is considered as the active site for Ni single-atom-based CO_2RR electrocatalysts.[21]

The CO_2RR performance of Ni–SAs–NC was evaluated in an H-type electrocatalytic cell with a standard three-electrode system, in which a platinum net and Ag/AgCl (3 M KCl) were used as the counter and reference electrodes, respectively. CO_2-saturated 0.5 M $KHCO_3$ was used as the electrolyte. Linear sweep voltammetry (LSV) curves of the samples were obtained on a rotating disc electrode at a rotation speed of 1600 r.m.p. As shown in Fig. 3a, unlike Ni–NPs–NC and NC, Ni–SAs–NC delivers much higher current densities under a CO_2 atmosphere in comparison with those under a N_2 atmosphere, indicating the efficient occurrence of the CO_2RR.[35] Meanwhile, Ni–SAs–NC can exhibit a much positive onset potential and a higher current density than Ni–NPs–NC and NC, suggesting that the Ni species, especially Ni–N_4 centers, are the more favorable active sites for the CO_2RR. Notably, NC, without Ni, exhibited negligible current densities. Therefore, Ni particles play an important role in electron transfer.

During the CO_2RR process, the gaseous and liquid products were quantitatively analyzed by on-line gas chromatography (GC) and ion chromatography, respectively. CO and H_2 are the only detected products in the applied potential range from −0.5 to −1.2 V. As shown in Fig. 3b, NC exhibits negligible activity for the conversion of CO_2 into CO. After anchoring Ni single atoms, the as-prepared Ni–SAs–NC has a maximum faradaic efficiency of CO (FE_{CO}) of up to 98% at −0.65 V, corresponding to an overpotential of 540 mV, and can maintain the high FE_{CO} exceeding 90% in an extensive potential range from −0.6 to −1.0 V. In contrast, Ni–NPs–NC only shows the highest FE_{CO} of 85% at −0.9 V, and maintains the high FE_{CO} in narrow potential points. Furthermore, Ni–SAs–NC could deliver a CO partial current density (j_{CO}) of up to 31 mA cm^{-2} at −0.96 V, which is much higher than those of Ni–NPs–NC and NC. Tafel plots of the samples were obtained based on their j_{CO} (Fig. 3c). As shown in Fig. 3d, Ni–SAs–NC exhibits a lower Tafel slope (127.6 mV dec^{-1}) than Ni–NPs–NC (155.0 mV dec^{-1}) and NC (306.5 mV dec^{-1}), indicating favorable reaction kinetics. Meanwhile, the values of the Tafel slopes for Ni–SAs–NC and Ni–NPs–NC are close to 118 mV dec^{-1}, implying that the first electron transfer process is the rate-determining step for CO generation.[36] In addition, Ni–SAs–NC possesses a higher electrochemically active surface area than Ni–NPs–NC and NC (Fig. S7†), revealing that Ni–SAs–NC possesses more active sites.[37,38] The favorable reaction kinetics and highly exposed active sites may promote the CO_2RR activity for Ni–SAs–NC. Besides the excellent CO_2RR activity, Ni–SAs–NC also exhibits conspicuous long-term stability. As shown in Fig. 3e, Ni–SAs–NC can deliver a steady current

density and a high FE_{CO} at −0.65 V during 30 hour electrocatalysis. Moreover, HAADF-STEM was conducted to determine the origin of the performance stability (Fig. S8†). The Ni atoms in Ni–SAs–NC can maintain their atomic dispersion state finely after the stability test without obvious agglomeration, and can eventually lead to good electrochemical stability.[39,40] Consequently, the excellent CO_2RR performance makes Ni–SAs–NC one of the most promising Ni single-atom based CO_2RR electrocatalysts (Fig. 3f and Table S3†).

4. Conclusions

In summary, a Ni single-atom catalyst named Ni–SAs–NC was prepared by a facile two-step process involving ingenious Ni-based precursor assembly and a simple one-step pyrolysis process. ICP-AES indicates that a high loading (2.0 wt%) of Ni can be achieved in Ni–SAs–NC. HAADF-STEM images and XPS, XANES and EXAFS spectra demonstrate that highly dense Ni active sites with the coordination structure of $Ni–N_4$ were atomically dispersed in Ni–SAs–NC, which consequently endow the as-prepared Ni–SAs–NC with outstanding electrocatalytic CO_2RR properties. Notably, the faradaic efficiency for CO generation can exceed 90% in a wide potential range from −0.6 to −1.0 V. Meanwhile, Ni–SAs–NC can also deliver a high CO partial current density and outstanding long-term stability. This work provides a cost-effective way to prepare a Ni-based single-atom electrocatalyst with excellent CO_2RR performance for CO production and inspires the exploration of high-efficiency single-atom catalysts for electrochemical applications.

Conflicts of interest

We declare that there are no conflicts of interest.

Acknowledgements

The authors acknowledge the financial support from the National Natural Science Foundation of China (No. 51772291, 21673238 and 21773242) and the Strategic Priority Research Program of the Chinese Academy of Sciences (No. XDB20000000). The authors thank Prof. B. Zhang from the Analysis and Test Center of Chongqing University for HAADF characterization, Prof. Y.-L. Chueh from National Tsing Hua University for TEM measurements, and Prof. L. Zheng from the Beijing Synchrotron Radiation Facility, Institute of High Energy Physics, Chinese Academy of Sciences, for the XANES and EXAFS experiments.

Notes and references

1 T. DeVries, M. Holzer and F. Primeau, Recent increase in oceanic carbon uptake driven by weaker upper-ocean overturning, *Nature*, 2017, **542**, 215–218.
2 A. J. Martín, G. O. Larrazábal and J. Pérez-Ramírez, Towards sustainable fuels and chemicals through the electrochemical reduction of CO_2: lessons from water electrolysis, *Green Chem.*, 2015, **17**, 5114–5130.
3 W. Ren, X. Tan, W. Yang, C. Jia, S. Xu, K. Wang, S. C. Smith and C. Zhao, Isolated diatomic Ni–Fe metal–nitrogen sites for synergistic electroreduction of CO_2, *Angew. Chem., Int. Ed.*, 2019, **58**, 6972–6976.
4 Q. Zhu, X. Sun, D. Yang, J. Ma, X. Kang, L. Zheng, J. Zhang, Z. Wu and B. Han, Carbon dioxide electroreduction to C_2 products over copper-cuprous oxide derived from electrosynthesized copper complex, *Nat. Commun.*, 2019, **10**, 3851.
5 H. Yang, Y. Wu, G. Li, Q. Lin, Q. Hu, Q. Zhang, J. Liu and C. He, Scalable production of efficient single-atom copper decorated carbon membranes for CO_2 electroreduction to methanol, *J. Am. Chem. Soc.*, 2019, **141**, 12717–12723.
6 A. Thevenon, A. Rosas-Hernandez, J. C. Peters and T. Agapie, *In situ* nanostructuring and stabilization of polycrystalline copper by an organic salt additive promotes electrocatalytic CO_2 reduction to ethylene, *Angew. Chem., Int. Ed.*, 2019, **58**, 16952–16958.
7 Q. He, D. Liu, J. H. Lee, Y. Liu, Z. Xie, S. Hwang, S. Kattel, L. Song and J. G. Chen, Electrochemical conversion of CO_2 to syngas with controllable CO/H_2 ratios over Co and Ni single-atom catalysts, *Angew. Chem., Int. Ed.*, 2020, **59**, 3033–3037.
8 D. Yang, Q. Zhu, X. Sun, C. Chen, W. Guo, G. Yang and B. Han, Electrosynthesis of a defective indium selenide with 3D structure on a substrate for tunable CO_2 Electroreduction to Syngas, *Angew. Chem., Int. Ed.*, 2020, **59**, 2354–2359.
9 W. Zhu, R. Michalsky, O. Metin, H. Lv, S. Guo, C. J. Wright, X. Sun, A. A. Peterson and S. Sun, Monodisperse Au nanoparticles for selective electrocatalytic reduction of CO_2 to CO, *J. Am. Chem. Soc.*, 2013, **135**, 16833–16836.
10 H. Mistry, Y. W. Choi, A. Bagger, F. Scholten, C. S. Bonifacio, I. Sinev, N. J. Divins, I. Zegkinoglou, H. S. Jeon, K. Kisslinger, E. A. Stach, J. C. Yang, J. Rossmeisl and B. Roldan Cuenya, Enhanced carbon dioxide electroreduction to carbon monoxide over defect-rich plasma-activated silver catalysts, *Angew. Chem., Int. Ed.*, 2017, **56**, 11394–11398.
11 A. Goyal, G. Marcandalli, V. A. Mints and M. T. M. Koper, Competition between CO_2 reduction and hydrogen evolution on a gold electrode under well-defined mass transport conditions, *J. Am. Chem. Soc.*, 2020, **142**, 4154–4161.
12 Q. Lei, H. Zhu, K. Song, N. Wei, L. Liu, D. Zhang, J. Yin, X. Dong, K. Yao, N. Wang, X. Li, B. Davaasuren, J. Wang and Y. Han, Investigating the origin of enhanced C_{2+} selectivity in oxide-/hydroxide-derived copper electrodes during CO_2 electroreduction, *J. Am. Chem. Soc.*, 2020, **142**, 4213–4222.
13 J. L. DiMeglio and J. Rosenthal, Selective conversion of CO_2 to CO with high efficiency using an inexpensive bismuth-based electrocatalyst, *J. Am. Chem. Soc.*, 2013, **135**, 8798–8801.

14 J. He, N. J. J. Johnson, A. Huang and C. P. Berlinguette, Electrocatalytic alloys for CO_2 reduction, *ChemSusChem*, 2018, **11**, 48–57.
15 J. Gu, C. S. Hsu, L. Bai, H. M. Chen and X. Hu, Atomically dispersed Fe^{3+} sites catalyze efficient CO_2 electroreduction to CO, *Science*, 2019, **364**, 1091–1094.
16 C.-Z. Yuan, S.-L. Zhong and A.-W. Xu, Powerful CO_2 electroreduction performance with N–carbon doped with single Ni atoms, *Catal. Sci. Technol.*, 2019, **9**, 3669.
17 T. Zheng, K. Jiang, N. Ta, Y. Hu, J. Zeng, J. Liu and H. Wang, Large-scale and highly selective CO_2 electrocatalytic reduction on nickel single-atom catalyst, *Joule*, 2019, **3**, 265–278.
18 Z. Zhang, J. Xiao, X.-J. Chen, S. Yu, L. Yu, R. Si, Y. Wang, S. Wang, X. Meng, Y. Wang, Z.-Q. Tian and D. Deng, Reaction mechanisms of well-defined metal-N_4 sites in electrocatalytic CO_2, *Angew. Chem., Int. Ed.*, 2018, **57**, 16339–16342.
19 X. Su, X. F. Yang, Y. Huang, B. Liu and T. Zhang, Single-atom catalysis toward efficient CO_2 conversion to CO and formate products, *Acc. Chem. Res.*, 2019, **52**, 656–664.
20 Y. Peng, B. Lu and S. Chen, Carbon-supported single atom catalysts for electrochemical energy conversion and storage, *Adv. Mater.*, 2018, **30**, 1801995.
21 S. Liu, H. B. Yang, S. F. Hung, J. Ding, W. Cai, L. Liu, J. Gao, X. Li, X. Ren, Z. Kuang, Y. Huang, T. Zhang and B. Liu, Elucidating the electrocatalytic CO_2 reduction reaction over a model single-atom nickel catalyst, *Angew. Chem., Int. Ed.*, 2020, **59**, 798–803.
22 K. Jiang, S. Siahrostami, A. J. Akey, Y. Li, Z. Lu, J. Lattimer, Y. Hu, C. Stokes, M. Gangishetty, G. Chen, Y. Zhou, W. Hill, W.-B. Cai, D. Bell, K. Chan, J. K. Nørskov, Y. Cui and H. Wang, Transition-metal single atoms in a graphene shell as active centers for highly efficient artificial photosynthesis, *Chem*, 2017, **3**, 950–960.
23 X.-M. Hu, H. H. Hval, E. T. Bjerglund, K. J. Dalgaard, M. R. Madsen, M.-M. Pohl, E. Welter, P. Lamagni, K. B. Buhl, M. Bremholm, M. Beller, S. U. Pedersen, T. Skrydstrup and K. Daasbjerg, Selective CO_2 reduction to CO in water using earth-abundant metal and nitrogen-doped carbon electrocatalysts, *ACS Catal.*, 2018, **8**, 6255–6264.
24 C. Yan, H. Li, Y. Ye, H. Wu, F. Cai, R. Si, J. Xiao, S. Miao, S. Xie, F. Yang, Y. Li, G. Wang and X. Bao, Coordinatively unsaturated nickel–nitrogen sites towards selective and high-rate CO_2 electroreduction, *Energy Environ. Sci.*, 2018, **11**, 1204–1210.
25 P. Shao, L. Yi, S. Chen, T. Zhou and J. Zhang, Metal-organic frameworks for electrochemical reduction of carbon dioxide: the role of metal centers, *J. Energy Chem.*, 2020, **40**, 156–170.
26 Y. N. Gong, L. Jiao, Y. Qian, C. Y. Pan, L. Zheng, X. Cai, B. Liu, S. H. Yu and H. L. Jiang, Regulating the coordination environment of MOF-templated single-atom nickel electrocatalysts for boosting CO_2 reduction, *Angew. Chem., Int. Ed.*, 2020, **59**, 2705–2709.
27 E. Zhang, T. Wang, K. Yu, J. Liu, W. Chen, A. Li, H. Rong, R. Lin, S. Ji, X. Zheng, Y. Wang, L. Zheng, C. Chen, D. Wang, J. Zhang and Y. Li, Bismuth single atoms resulting from transformation of metal-organic frameworks and their use as electrocatalysts for CO_2 reduction, *J. Am. Chem. Soc.*, 2019, **141**, 16569–16573.
28 A. V. Desai, B. Manna, A. Karmakar, A. Sahu and S. K. Ghosh, A water-stable cationic metal-organic framework as a dual adsorbent of oxoanion pollutants, *Angew. Chem., Int. Ed.*, 2016, **55**, 7811–7815.
29 H. B. Yang, S.-F. Hung, S. Liu, K. Yuan, S. Miao, L. Zhang, X. Huang, H.-Y. Wang, W. Cai, R. Chen, J. Gao, X. Yang, W. Chen, Y. Huang, H. M. Chen, C. M. Li, T. Zhang and B. Liu, Atomically dispersed Ni(i) as the active site for electrochemical CO_2 reduction, *Nat. Energy*, 2018, **3**, 140–147.
30 Q. Wu, J. Gao, J. Feng, Q. Liu, Y. Zhou, S. Zhang, M. Nie, Y. Liu, J. Zhao, F. Liu, J. Zhong and Z. Kang, A CO_2 adsorption dominated carbon defect-based electrocatalyst for efficient carbon dioxide reduction, *J. Mater. Chem. A*, 2020, **8**, 1205–1211.
31 H. Yang, Q. Lin, C. Zhang, X. Yu, Z. Cheng, G. Li, Q. Hu, X. Ren, Q. Zhang, J. Liu and C. He, Carbon dioxide electroreduction on single-atom nickel decorated carbon membranes with industry compatible current densities, *Nat. Commun.*, 2020, **11**(1), 593.
32 L. Ye, Y. Ying, D. Sun, Z. Zhang, L. Fei, Z. Wen, J. Qiao and H. Huang, Highly efficient porous carbon electrocatalyst with controllable N-species content for selective CO_2 reduction, *Angew. Chem., Int. Ed.*, 2020, **59**, 3244–3251.
33 J. Xu, Y. Kan, R. Huang, B. Zhang, B. Wang, K. H. Wu, Y. Lin, X. Sun, Q. Li, G. Centi and D. Su, Revealing the origin of activity in nitrogen-doped nanocarbons towards electrocatalytic reduction of carbon dioxide, *ChemSusChem*, 2016, **9**, 1085–1089.
34 M. Jia, C. Choi, T. S. Wu, C. Ma, P. Kang, H. Tao, Q. Fan, S. Hong, S. Liu, Y. L. Soo, Y. Jung, J. Qiu and Z. Sun, Carbon-supported Ni nanoparticles for efficient CO_2 electroreduction, *Chem. Sci.*, 2018, **9**, 8775–8780.
35 C. Cao, D. D. Ma, J. F. Gu, X. Xie, G. Zeng, X. Li, S. G. Han, Q. L. Zhu, X. T. Wu and Q. Xu, Metal-Organic Layers Leading to Atomically Thin Bismuthene for Efficient Carbon Dioxide Electroreduction to Liquid Fuel, *Angew. Chem., Int. Ed.*, 2020, **59**, 15014–15020.
36 C. Z. Yuan, H. B. Li, Y. F. Jiang, K. Liang, S. J. Zhao, X. X. Fang, L. B. Ma, T. Zhao, C. Lin and A.-W. Xu, Tuning the activity of N-doped carbon for CO_2 reduction via in situ encapsulation of nickel nanoparticles into nano-hybrid carbon substrates, *J. Mater. Chem. A*, 2019, **7**, 6894–6900.
37 P. Su, K. Iwase, S. Nakanishi, K. Hashimoto and K. Kamiya, Nickel-nitrogen-modified graphene: an efficient electrocatalyst for the reduction of carbon dioxide to carbon monoxide, *Small*, 2016, **12**, 6083–6089.
38 H. Li, N. Xiao, M. Hao, X. Song, Y. Wang, Y. Ji, C. Liu, C. Li, Z. Guo, F. Zhang and J. Qiu, Efficient CO_2 electroreduction over pyridinic-N active sites highly exposed on wrinkled

porous carbon nanosheets, *Chem. Eng. J.*, 2018, **351**, 613–621.

39 X. Li, W. Bi, M. Chen, Y. Sun, H. Ju, W. Yan, J. Zhu, X. Wu, W. Chu, C. Wu and Y. Xie, Exclusive Ni-N4 Sites Realize Near-Unity CO Selectivity for Electrochemical CO_2 Reduction, *J. Am. Chem. Soc.*, 2017, **139**(42), 14889–14892.

40 X. Wang, Z. Chen, X. Zhao, T. Yao, W. Chen, R. You, C. Zhao, G. Wu, J. Wang, W. Huang, J. Yang, X. Hong, S. Wei, Y. Wu and Y. Li, Regulation of Coordination Number over Single Co Sites: Triggering the Efficient Electroreduction of CO_2, *Angew. Chem., Int. Ed.*, 2018, **57**, 1944–1948.